Phase Behaviors of Charged Star Block Copolymers at Fluids Interface

Zhan Chen[a], Alexander E. Ribbe[a], Christian Steinmetz[a], E. Bryan Coughlin[a], Mingqiu Hu[a], Xuchen Gan[a], Thomas P. Russell*[a],[b]

[a] Z. Chen, Dr. A. E. Ribbe, Dr. C. Steinmetz, Prof. E. B. Coughlin, M. Hu, X. Gan, Prof. T.P. Russell
Department of Polymer Science and Engineering
University of Massachusetts Amherst
Amherst, MA 01003 (USA)
E-mail: russell@mail.pse.umass.edu

[b] Prof. T. P. Russell
Material Science Division
Lawrence Berkeley National Laboratory
Cyclotron Road, Berkeley, CA 94720 (USA)

Supporting information for this article is given via a link at the end of the document.

Abstract: The phase behaviors of block copolymers (BCPs) at the water-oil interface are influenced by the segmental interaction parameter (□) and chain architecture. We synthesized a series of star block copolymers (s-BCPs) having polystyrene (PS) as core and poly(2-vinylpyridine) (P2VP) as corona. The interaction parameters of block-block ($□_{PS\text{-}P2VP}$) and block-solvent ($□_{P2VP\text{-}solvent}$) were varied by adjusting the pH of the aqueous solution. Lowering pH increased the fraction of quaternized-P2VP (Q-P2VP) with enhanced hydrophilicity. By transferring the equilibrated interfacial assemblies, morphologies ranging from bicontinuous films at pH of 7 and 3.1 to nanoporous and nanotubular structure at pH of 0.65 were observed. The nanoporous films formed hexagonally packed pores in s-BCP matrix, while nanotubes comprised Q-P2VP as corona and PS as core. Control over pore size, d-spacing between pores, and nanotube diameters was achieved by varying polymer concentration, molecular weight, volume fraction and arm number of s-BCPs. Large-scale nanoporous films were obtained by freeze-drying emulsions. Remarkably, the morphologies of linear BCPs were inverted, forming hexagonal-packed rigid spherical micelles with Q-P2VP as core and PS as corona in multilayer. This work provides insights of phase behaviors of BCP at fluids interface and offer a facile approach to prepare nanoporous film with well-controlled pore structure.

Introduction

The self-assembly of block copolymers (BCPs) in thin films is quite well-understood, which is fundamental to determining their potential applications in nanotemplating,[1] nanolithographic patterning,[2] membranes,[3] and photonic crystals.[4] The morphology and orientation of BCPs are key in this context. The morphology can be controlled by changing the volume fraction of each block, enabling the formation of lamellar, cylindrical, gyroid, and spherical morphologies.[5] Strategies for controlling the orientation of BCP microdomains in thin film include tuning (1) the interfacial interactions between blocks and the substrate;[6] (2) the surface energies of the blocks,[7] and (3) the frustration arising from the incommensurability of the film thickness and period of the BCP microdomain.[8] When the interactions of both blocks at the substrate/air interfaces are equal, there is no preferential wetting, and the microdomains orient normal to the substrate, particularly when the film thickness is incommensurate with the period of the BCP microdomain.[6-7] With a preferential interaction of one block with the substrate, or, if one block has a lower surface energy, the microdomain morphology will orient parallel to the interface and propagate throughout the entire film.[9]

The self-assembly of BCPs at homopolymer interfaces has also been widely investigated, with the assembly of the BCPs to the interface and a segregation of the blocks into the homopolymers with which they are miscible.[10] This results in a broadening of the interface between the homopolymers and an increase of the adhesion, making the BCPs useful as compatibilizers for polymer recycling and upcycling.[11] Detailed insights into the assembly of BCPs at homopolymer interfaces have been obtained by neutron reflectivity,[12] dynamic secondary ion mass spectroscopy,[13] and forward recoil spectroscopy,[14] where quantitative segmental density profiles of the BCPs and homopolymers at the interface have been obtained.

BCPs can also segregate at fluid interfaces, acting as emulsifiers, with the hydrophobic and hydrophilic blocks residing in the oil and aqueous phases, respectively, thereby reducing the interfacial energy between the two fluids.[15]. In comparison to a homopolymer interface, there is a much broader range in block-solvent interactions ($□_{block\text{-}solvent}$) at fluid interfaces, leading to more variable phase behavior.[16] For example, BCPs can be made responsive to changes in pH,[16a, 17] ionic strength,[18] light,[19] temperature,[20] and chemicals[21]

that can induce changes in the chemical identity or configuration of the BCPs, all of which can result in significant changes in the phase behavior.

In addition, a more complex architecture of BCPs, such as star or bottlebrush copolymers, can impose further constraints on the interfacial behavior.[16a, 22] Chemically joining multiple linear diblock copolymers to a central point or sequentially along a linear backbone chain yields star or bottlebrush block copolymers, respectively.[23] The molecular architecture not only influences the entropy of the polymer chain, but also influences the enthalpic interactions between the segments by biasing the spatial location of the different blocks and interactions between blocks and the solvents, e.g., the architecture can limit the access of the solvent to the blocks.[22a] The connectivity of the BCP chains in advanced architectures leads to kinetically-trapped and equilibrated conformations from coordination between multiple chains.[22] Thus, the interaction of blocks with a favorable solvent may be limited by their neighbors, where entropy plays a critical role in the equilibrium phase behavior. For example, it was found that lowering grafting density of random bottlebrush copolymer that was synthesized from randomly distributing two homopolymer chains along the backbone yielded lower interfacial tension compared to a bottlebrush with 100% grafting density, due to the improved wetting of solvents and the side chain.[22a]

In this work, we describe the phase behavior of star block copolymers (s-BCPs) at the water-oil interface by transferring interfacial assemblies from the water-oil interface to the silicon substrate. A series of s-BCPs, having polystyrene as the core block and P2VP as the corona block, were synthesized, where the arm number, volume fractions of arm components, and molecular weights were varied. The interactions between P2VP and the aqueous phase is modulated by adjusting the pH of the aqueous solution, where P2VP can be converted to quaternized P2VP (Q-P2VP) under acidic conditions.[16, 24] When the pH decreases, the protonation level of P2VP increases (increasing Q-P2VP fraction), enhancing electrostatic interactions between molecules and increasing the Flory-Huggins interaction parameter (χ) between the two blocks.[24-25] It was shown that the interfacial assemblies of s-BCPs formed bicontinuous films at neutral (pH=7), but the phases were reversed at pH =3.10. At a pH of 0.65, where the degree of protonation is highest, nanoporous films and nanotube morphologies were identified. The assembly mechanisms of nanoporous film and nanotube morphologies were investigated by transmission electron microscopy (TEM) and cross-section scanning electron microscopy (SEM), where thicker interfacial assemblies (a few hundred nm) are composed of hexagonally packed pores in the s-BCPs matrix, while free s-BCPs comprise the nanotube in thinner assemblies (~10 nm) with Q-P2VP as corona and PS as the core. We demonstrate the ability to control the phase behavior by varying polymer concentration, molecular weight (MW), volume fraction, and architecture. The large-scale nanoporous film was prepared via freeze-dried emulsion, showing hexagonally packed air pores in the s-BCPs matrix at 3-dimension manner. Notably, when the linear diblock copolymers are used, the nanoporous film morphology inverts, with hard spherical micelle crystalize in multilayers at fluids interface.

Results and Discussion

Interfacial Assemblies Transferred from the Water-Oil Interface

Table 1 details the star block copolymers (s-BCPs) used in this study, having polystyrene (S) as the core block and poly(2-vinylpyridine) (V) as the corona block. These were synthesized by a “grafting from” approach using reversible addition-fragmentation chain-transfer (RAFT) polymerization. We have previously published a more detailed description of the synthetic steps to prepare these s-BCPs.[16a, 26] In the present study, 1-arm s-BCPs (diblocks) to 2-arm s-BCP (triblocks), 3-arm s-BCPs, and 4-arm s-BCPs were investigated. As shown in Figure S1, the s-BCPs had similar arm periods across different architectures, which is evidenced by the comparable lamellar periods (L) shown in their bulk morphologies, as determined by small-angle X-ray scattering (SAXS).[26] We assume that each arm period is approximately one-half the lamellar period (L/2). For all symmetric s-BCPs, the PS and P2VP microdomains have the same volume fraction in the bulk, as indicated by the absence of 2q* (even order reflections) in the SAXS profiles. For the asymmetric s-BCPs, (S94-*b*-V26)$_4$ has only one broad peak, while (S94-*b*-V153)$_4$ forms a lamellar microdomain morphology with unequal sizes of the microdomains (in presence of 2q*).

Table 1. Characteristic of star block copolymers (S-*b*-V)$_n$

Code	PS block M_n [g mol^{-1}][a]	PS block DP_n per arm	f_{PS} by NMR [b]	P2VP block M_n [g mol^{-1}][c]	P2VP block DP_n per arm	Total M_n [g mol^{-1}]	$Đ$[d]
(S125-*b*-V124)$_1$	13000	125	0.52	13000	125	26000	1.04
(S88-*b*-V93)$_2$	18240	88	0.51	19600	93	37840	1.37

(S98-*b*-V103)$_3$	30600	98	0.51	32500	103	63100	1.34
(S150-*b*-V162)$_3$	46900	150	0.51	51100	162	98000	1.15
(S27-*b*-V40)$_4$	11300	27	0.42	16800	40	28100	1.12
(S94-*b*-V26)$_4$	39300	94	0.80	10900	26	50200	1.16
(S94-*b*-V99)$_4$	39300	94	0.51	41600	99	80900	1.46
(S94-*b*-V153)$_4$	39300	94	0.40	64300	153	103600	1.32

[a] Calculated from size exclusion chromatography (SEC) in dimethylformamide using PS calibration. [b] Calculated from volume fractions. [c] Calculated from f_{PS}. [d] Determined from size exclusion chromatography (SEC) in dimethylformamide using PS calibration. [e] Purchased from Polymer Source. Inc

As shown in Scheme 1, using the 4-arm s-BCPs as an example, interfacial assemblies were prepared by placing a toluene solution of the s-BCPs on top of an aqueous phase where the pH was adjusted by the addition of hydrochloric acid (HCl), and aged for one hour to equilibrate the bilayer system. Subsequently, the s-BCP solution was replaced with pure toluene, leaving only the s-BCP assemblies at the interface. The interfacial assemblies were then transferred to a silicon wafer, followed by an air-drying process.

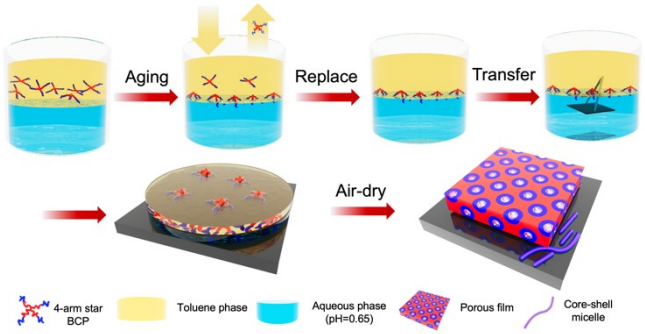

Scheme 1. The interfacial assemblies of star block copolymers (s-BCPs) transferred from the water-oil interfaces. s-BCPs dissolved in toluene solution were placed atop of aqueous solution with different pH. After aging 1 h to reach equilibrium of assemblies, s-BCPs solution was replaced by pristine toluene, where s-BCPs were only remained at fluids interface. The interfacial assemblies were further transferred by silicon wafer, followed by an air-drying process.

pH-Dependent Morphologies of Interfacial Assemblies

By altering the pH of the aqueous solution, we can effectively control the interactions of the P2VP block with the aqueous phase ($\chi_{P2VP\text{-}solvent}$), due to the pH-dependent change in the degree of protonation of P2VP.[16a, 25] Lowering the pH results in an increased degree of protonation.[24] This amplifies the electrostatic interactions and increases the χ between PS and P2VP, leading to different morphologies at the interface. As shown in Figure S2, with an aqueous phase of pure water (neutral) and a pH of 3.10 (regulated by HCl), a bicontinuous morphology is observed. The thickness of the transferred interfacial layer increases from 2.8 nm to 4.3 nm as the aqueous phase is adjusted from pure water to a pH of 3.10. This increase is attributed to the enhanced amphiphilic character of the s-BCPs, which leads to an increased number of s-BCPs at the interface. Reducing the pH further to 0.65 (degree of protonation is ~1) results in two distinct morphologies, as is evident from the AFM image in Figure S3: The assemblies consist of a thick (~200 nm) film, with a much thinner "film"(~10 nm) in the periphery. We note that concentration can be used to vary the thickness of thick film. Distinctly different morphologies are observed in these two areas. The thick films appear nanoporous, with hexagonally packed pores (Figure 1a) in the s-BCPs matrix. The pore diameter and depth are measured from Figure 1b as 59±11 nm and 8±3 nm, respectively. As depicted in Figure 1c, the thinner area consists of long tubules, with 9±1 nm in height, 49±7 nm in width, and microns in length. Even though these tubules are closely aligned with their neighbors, they did not coalesce. These tubules can form large bending angles due to the high aspect ratio. The interfacial assemblies were characterized using grazing-incidence small-angle X-ray scattering (GISAXS). In Figure 1e, the mixed morphologies (including the nanoporous film and nanotubules) yield a pronounced in-plane peak with a d-spacing of 84.0 nm, arising from the contrast between the air-filled pores and the polymer matrix. A Fast Fourier transform (FFT) of the images in Figure 1a show a characteristic spacing of 85 nm, which agrees with GISAXS results. For short aging times of 5 min, one finds similar morphologies but with a lower degree order (Figure S4).

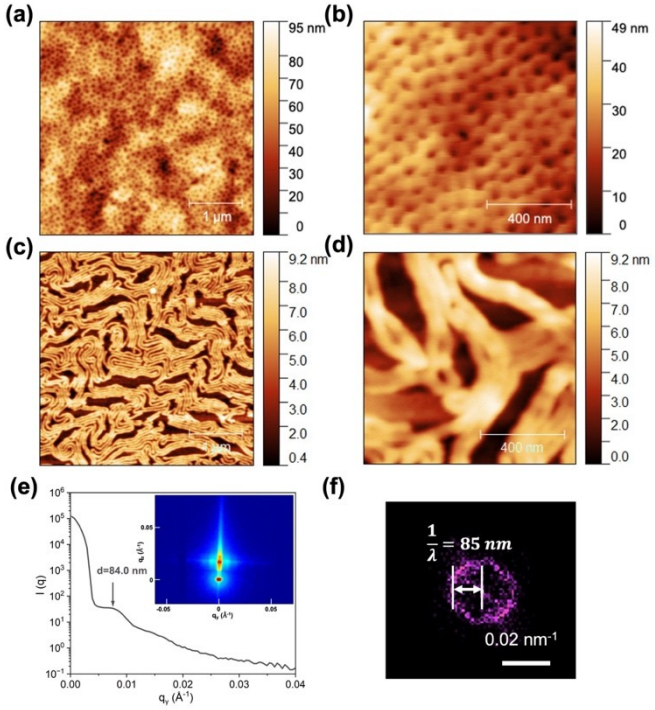

Figure 1. The nanoporous and nanotubular morphologies from interfacial assemblies of 4-arm star block copolymers (s-BCPs) at the water-oil interface. Different size scale of atomic force microscopy (AFM) height images for a) and b): nanoporous morphologies and c) and d): nanotube morphology. The nanoporous morphologies show hexagonally packed pores with an average pore diameter of 59±11 nm, while well-defined nanotubes (microns in length) with an average tube diameter of 49±7 nm are observed in the thinner portions of the film. e) GISAXS of transferred interfacial assemblies at incident angle 0.18 with 900 s exposure time. The primary reflection has a d-spacing of 84.0 nm (calculated by $d=2\pi/q^{*}$). f) Fast Fourier transform (FFT) of a) exhibits a maximum at a d-spacing of 85.0 nm, consistent with GISAXS results. These studies used a 0.1 mg/ml of (S94-*b*-V99)$_4$ solution in toluene, with an aqueous phase pH of 0.65 using HCl. The interfacial assemblies were transferred after aging for 1h.

The Mechanism for the Formation of Nanoporous and Nanotubular Morphologies

A similar behavior is seen for 3-arm s-BCPs. Figure S5 shows the interfacial assemblies of (S150-*b*-S162)$_3$, with both nanoporous and nanotubular morphologies. The pore and tube diameters are measured as 68±9 nm and 49±5 nm, respectively. The d-spacing between pores is found to be 87 nm from GISAXS measurements. Given the well-defined length scales of these morphologies, assessing the length scales associated with the conformation of the s-BCPs is important in understanding the mechanism underlying both morphologies. The increase of interaction parameter between the P2VP blocks and solvents ($\chi_{P2VP\text{-}solvent}$) at the acidic aqueous phase would cause a significant stretching of the Q-P2VP, making L/2 of bulk s-BCP a lower limit of the projected length of the s-BCP normal to the interface. Previously, we investigated the bulk morphology of the same s-BCPs doped with 10% $CuCl_2$ and established a linear relationship between L and the MW of the arms. From this, we argued that the L/2 of (S150-*b*-V162)$_3$ would increase to ~17 nm when doped with 10% $CuCl_2$, compared to 12.2 nm without doping. While this is not a direct measure of the charged s-BCP arm length at fluid interface, it provides a useful reference for understanding the characteristic lengths in the nanoporous and nanotubular morphologies.

We used TEM to locate the PS and P2VP blocks in the phase-separated morphologies. We first confirmed that interfacial assemblies transferred onto Au grids replicated the topographical morphologies observed via AFM on Si wafers (Figure S7). As shown in Figure 2b, the nanotube diameter was found to be 40±3 nm, in agreement with the AFM results. In all the morphologies, a darker corona and lighter core were observed, indicating that nanotubes have a corona of chloride containing Q-P2VP and a core of PS. We also observed single spherical micelles, pairs of spherical micelles (micelles making contact while others were coalescing), clusters of three droplets after coalescence, and linear tubes formed from the successive coalescence of multiple spherical micelles. The diameters of the tubes are ~43 nm, indicating that they are formed by coalescence of two s-BCPs in radial direction, with solvated PS cores, upon first drying of the toluene, causing the formation of the tubular structures (Figure 2a). The areal density of the copolymers assembled on the surface of the micelles increases as the toluene evaporates, preventing a 3D coalescence, as shown in Figure 2a and 2c. This increased areal density of the s-BCPs and the charged nature of the P2VP on the surface of the tubules, prevents a coalescence and leads to the apparent alignment or stacking of the tubules as the water evaporates (Figure 2d). Surprisingly, these nanotubules can form rings, showing the same contrast in TEM (Figure 2e) as their linear counterparts, though their diameter is much smaller, measured as 27±3 nm (Figure 1e). While both the linear and ring nanotubular consist of bilayers, it is apparent from the TEM images that the contrast of the rings is less evident compared to linear structure, indicating lower areal density of for the rings, as schematized in Figure 2a. We can only speculate on the origin of the ring structure: these might arise from the residual water droplets on the surface during drying, which induces a curvature in tubules growing in opposite directions around the droplet.

While the tubular structures can be understood in terms of coalescence, that is not the case for the porous structures observed. Since the nanoporous film is an order of magnitude thicker than that of the nanotubes, the nanoporous morphology

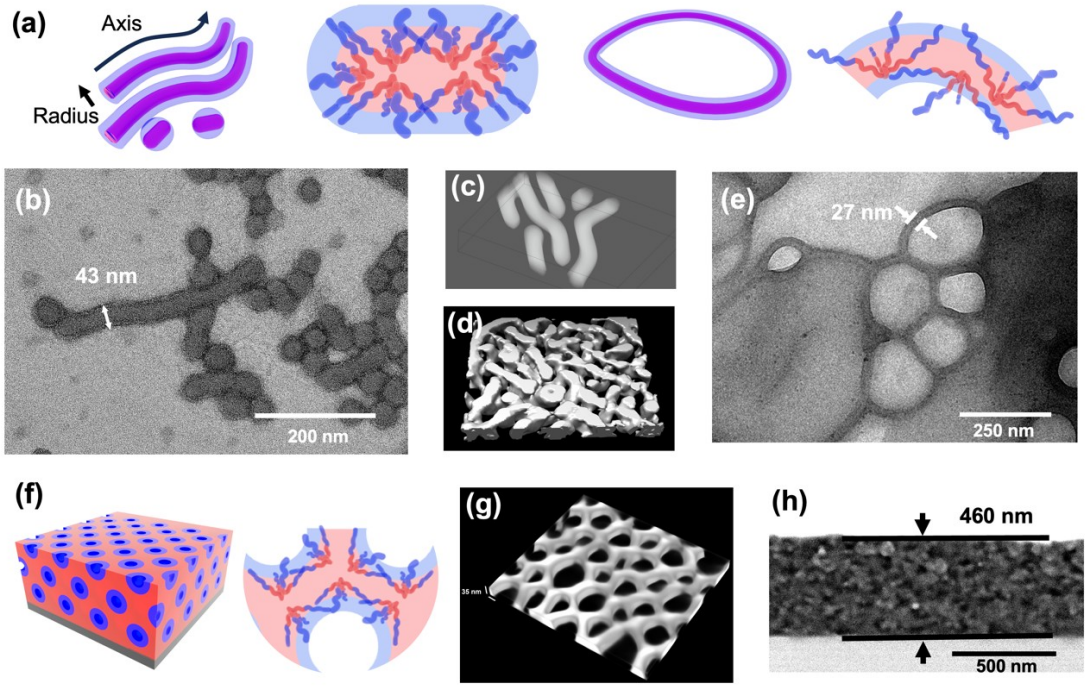

Figure 2. The mechanism of formation nanoporous and nanotubular morphology from transferred interfacial assemblies through electron microscopy visualization. a) Schematic illustration of linear and ring nanotube. b) Transmission electron microscopy (TEM) image of the linear nanotube, measuring 40±3 nm. TEM tomography of c) single layer and d) multilayer of the linear nanotube. e) TEM image of ring tube with measured diameter 27±3 nm. f) Schematic illustration of nanoporous morphology. g) TEM tomography of nanoporous film. h) Scanning electron microscopy (SEM) of cross-section nanoporous film using backscattering detector. the film thickness was measured as 460 nm. (b)-(e) used 0.1 mg/ml $(S150\text{-}b\text{-}V162)_3$. (g) used 0.1 mg/ml $(S98\text{-}b\text{-}V103)_3$. (h) used 2 mg/ml $(S150\text{-}b\text{-}V162)_3$. pH=0.65 (HCl) is used as an aqueous phase. Interfacial assemblies are transferred after 1 h assembly at the fluids interface followed by air-dry.

must arise from larger scale assemblies of the s-BCPs at the fluid interface. As toluene evaporates more rapidly than water, the porous structures must form during the evaporation of the remaining water. This is further corroborated by AFM phase images (Figure S8) that P2VP block (the P2VP block has a smaller phase lag compared to the PS block[24]) coats the walls of the pores. We used TEM tomography to 3D reconstruct a single layer of a nanoporous film (Figure 2g). To visualize a cross-section of the film, we increased the concentration of $(S150\text{-}b\text{-}V162)_3$ from 0.1 mg/ml to 2 mg/ml in toluene. As seen in Figure S9, the average d-spacing between the pores decreased from 87 nm to 63 nm, as measured by the GISAXS. This indicates that increasing the concentration of s-BCPs can more efficiently stabilize the water droplet during evaporation, resulting in more densely packed air pores after the water is removed. The as-prepared transferred film was freeze fractured by immersion in liquid nitrogen and then examined by SEM equipped with a backscattered electron detector. As seen in Figure 2h, the nanoporous film has a uniform thickness of ~460 nm using a 2 mg/ml $(S150\text{-}b\text{-}S162)_3$. The presence of dark pores dispersed within the film can be attributed to voids, as voids do not generate backscattered electrons. From the microscopy results, we can deduce a mechanism by which the pores form. After transfer, toluene evaporates from the top of the film, increasing the concentration of water within the film which leads to the phase separation and formation of water droplets. The mobility of the s-BCPs is still high, allowing the assembly of the s-BCPs at the interface of the aqueous droplets within a hydrophobic (PS block in toluene) matrix to decrease interfacial energy. These surfactant-stabilized droplet reorganize and pack more efficiently into a hexagonal packing. As the toluene continues to evaporate, the glass transition temperature (T_g) of the matrix increases, locking the s-BCP-stabilized water droplets in-place. Subsequent evaporation of the water leaves behind pores that are hexagonally packed. This mechanism is further confirmed by performing the same experiments on transferred interfacial assembly dried at 65 °C or under vacuum to accelerate the evaporation process, where the results showed wrinkled film with a sparse distribution of pores (Figure S10). The wrinkling and sparse distribution of pores more than likely arises from the very rapid evaporation at the surface of the transferred film, forming a skin layer on top that swell as the solvent beneath surface further evaporate, which will induce compressive force among the film and eventually lead to wrinkles.

Morphology Control by Tuning Volume Fraction and Architecture

Since the nanoporous and nanotubular morphologies originate from interfacial assemblies of s-BCPs, their phase behaviors should be modulated by adjusting the molecular weight (MW), volume fractions, and architectures of s-BCPs. When the MWs of s-BCPs are reduced, bringing the s-BCPs into the weak segregation regime (Figure S11), the s-BCPs cannot stabilize water droplets and fail to form tubular structures and a homogeneous film is produced (Figure S12). Considering s-BCPs are synthesized by a "grafting from" method, a range of volume fractions of s-BCPs can be synthesized with identical PS block lengths but varying P2VP block lengths.[23a] As shown in Figure 3a, with (S94-*b*-V26)$_4$, like the low MW s-BCP in the weak segregation regime (Figure S1), the interfacial assemblies cannot stabilize the morphologies after drying, leaving homogeneous films with a sparse distribution of pores. Nevertheless, the intermolecular interactions (S94-*b*-V26)$_4$ remain sufficiently strong to form wrinkles when water droplets are trapped within the film (visible when the film is thin) (Figure 3b). When the P2VP block length is increased to (S94-*b*-V153)$_4$, due to the asymmetry of the PS and Q-P2VP blocks, water droplets are stabilized, but absent ordering (Figure 3c). The nanotubes formed with (S94-*b*-V153)$_4$ are seen to break up into fragments (Figure 3d and Figure S12). This can be attributed to Plateau-Rayleigh instabilities, where the imbalance in the amphiphilicity of s-BCPs leads to a break-up of the linear tubule.[27] Interestingly, when a water droplet is trapped within the center, it is easier for (S94-*b*-V153)$_4$ to maintain the integrity of the tubular ring. This might be due to the additional interfacial energy needed when a continuous (S94-*b*-V153)$_4$ ring breaks up, leaving a free water-air surface (Figure 3e and Figure S13). We also note that the tubular ring of (S94-*b*-V153)$_4$ has a diameter of 32 nm, smaller than the 45 nm of the linear tube, which is consistent with the results of (S94-*b*-V99)$_4$.

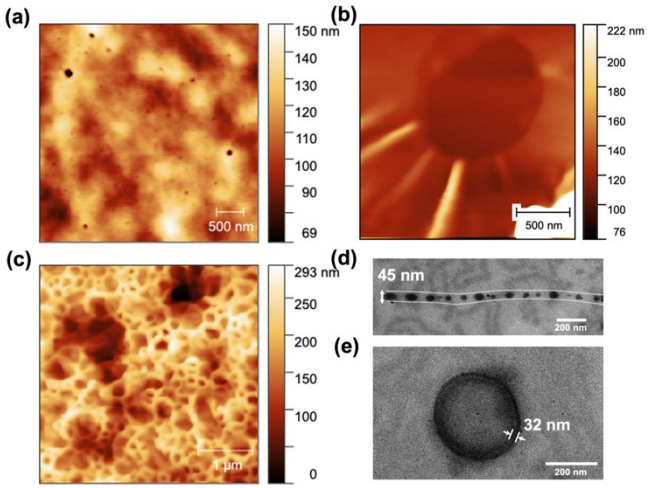

Figure 3. Controlling morphology variation through volume fraction adjustment of star block copolymers (s-BCPs). Atomic force microscopy (AFM) height image of a) A thick and b) a thin film of transferred interfacial assemblies derived from (S94-*b*-V26)$_4$. AFM height image of c) nanoporous structure. Transmission electron microscopy (TEM) image of d) fragmented nanotube and e) ring nanotube of transferred interfacial assemblies derived from (S94-*b*-V153)$_4$. Solutions of 0.1 mg/ml s-BCPs in toluene were used with a pH 0.65 aqueous solution (adjusted using HCl). The interfacial assemblies were transferred after 1 h assembly of s-BCPs at the fluids interface and subsequently air-dried.

Both the 3-arm s-BCPs (S98-*b*-V103)$_3$ and the 2-arm s-BCPs (triblock) (S88-*b*-V93)$_2$ showed hexagonally packed pores in thicker films and well-defined nanotubes for the much thinner "films" (Figure 4 and Figure S14). The pore diameters were measured as 49±8 nm and 35±6 nm for the 3-arm s-BCPs and triblock, with d-spacing (determined by FFT of AFM images) of 83 nm and 54 nm, respectively. Similarly, FFT of the TEM image

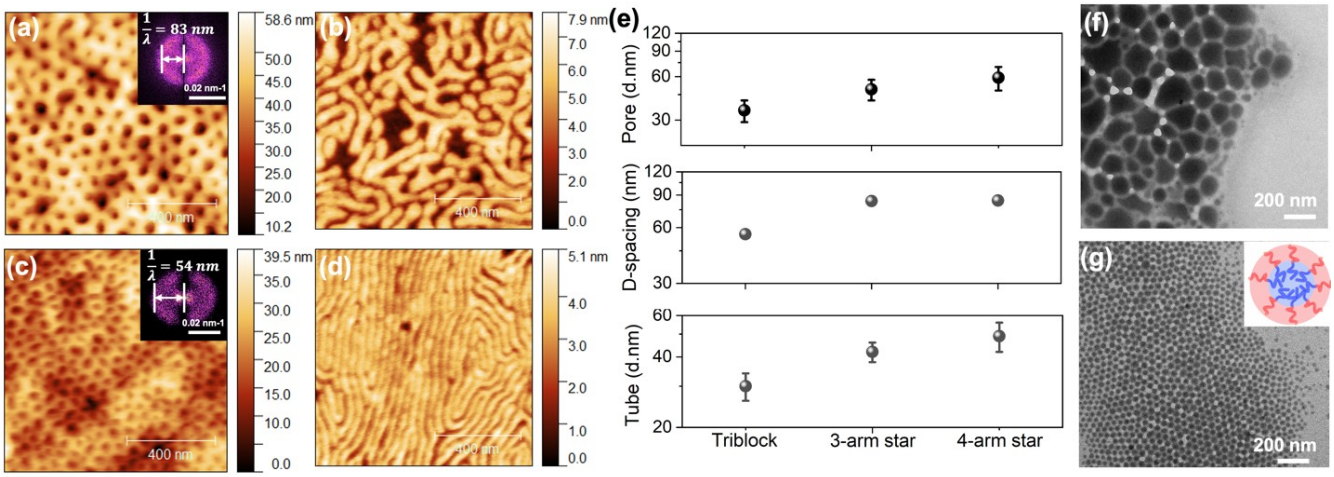

Figure 4. Influence of star block copolymer (s-BCP) architecture on the formation of nanoporous and nanotube morphologies. Atomic force microscopy (AFM) height images of a)-b) 2-arm s-BCPs (triblock) and c)-d) 3-arm BCPs. Insets: Fast Fourier transform of corresponding AFM images. e) Summary of the effects of s-BCP architecture on nanoporous and nanotube morphologies. Transmission electron microscopy (TEM) images of f) nanoporous and g) large domain formed from assemblies of a rigid spherical micelle of linear diblock BCPs. Linear diblock BCPs (S125-*b*-V124)$_1$, 2-arm BCPs (triblock, (S88-*b*-V93)$_2$), and 3-arm BCPs (S98-*b*-V103)$_3$ were used in this study. s-BCP solutions (0.1 mg/ml in

toluene) were combined with an aqueous solution of pH 0.65 (adjusted using HCl). After 1 h of s-BCP assembly at the fluid interface, the interfacial assemblies were transferred and air-dried.

yielded d-spacings of 75 nm and 49 nm, respectively (Figure S14), while GISAXS of the transferred films gives the values of 83 nm and 55 nm (Figure S14 and Figure S15). The diameters of the tubular structures were measured as 42±4 nm and 30±4 nm for 3-arm s-BCPs and triblock, respectively. These results are summarized in Figure 4e. As the arm number increases from 2 to 4, the diameter and the d-spacing of the pores increases. Previous reports on the comparable system indicated that the radius of gyration of s-BCPs at the fluid interface tends to increase with an increasing arm number when s-BCPs are highly charged, along with a higher interfacial tension.[16a] Consequently, the triblock is more effective in stabilizing water droplets, leading to the reduced pore diameter and d-spacing. The diameters of the tubules show the same architectural trend, with the triblock having the smallest value. This can be attributed to the softer nature of the triblock with only two charged arms, which do not stretch at the same degree as the 4-arm s-BCPs.[16a]

For linear diblock PS-*b*-P2VP copolymers, both the PS and P2VP blocks have one free chain end, resulting in either block can potentially constitute the corona of the micelle. As shown in Figure 4f, for the assemblies in the thicker films (nanoporous films), the darker area can be assigned to the Q-P2VP block with Cl^- counterions, while the brighter matrix is PS. Compared to the well-ordered porous structure observed in multi-arm BCPs, linear diblock BCPs do not promote well-ordered pores probably due to the lower interfacial binding energy. Unlike multi-arm BCPs, where the P2VP block forms the corona and PS comprise the cores of the nanotubules, linear diblock BCPs tend to form spherical micelles with the P2VP block serving as the core and PS as the corona, as evidenced by the darker core in TEM images (Figure 4g). Given that these spherical micelles exhibit a well-defined diameter of 37±5 nm and are rigid due to the charging of the P2VP block, they can order into larger domains.

Large scale nanoporous film preparation

There are limitations to producing a nanoporous films over a large area by interfacial transfer, as the transfer process can disrupt the interfacial assemblies, leading to a limited area being covered on the silicon substrate. Therefore, as shown in Figure 5a, we prepared interfacial assemblies by directly depositing a pH=0.65 aqueous phase onto the silicon substrate, then placing a toluene solution of (S94-*b*-V99)$_4$ on top. The interfacial assemblies are simply obtained once the toluene and water are removed. As shown in Figure 5b, we obtained a porous film with a larger pore size of 78±10 nm compared to that obtained by the interfacial transfer. We also placed a toluene solution of (S94-*b*-V99)$_4$ onto the wafer initially, then covered with a pH=0.65 aqueous phase. Since the toluene phase has a lower density (0.867g/cm^3) than the aqueous phase (0.997g/cm^3), it rises to the surface, increasing the exposure of the (S94-*b*-V99)$_4$ to the aqueous phase. As shown in Figure 5c, s-BCPs rigid spherical micelles developed rather than tubular structures, most likely due to the higher degree of charging of Q-P2VP. A nanoporous film can also be obtained by a breath figure method, with pore diameter measured as 79±18 nm (Figure S16).

Another strategy to create large-scale fluid interfacial assemblies involves the use of water-oil emulsions, where the total surface area of all the emulsion droplets is accumulated. This process is usually limited by the weak binding energy of BCPs to the interface or the weak intermolecular interactions, which may disrupt the integrity of the emulsion film after drying. This can be avoided by using PS-*b*-P2VP, which has a strong binding energy at fluid interfaces when P2VP is charged. We prepared a water-in-oil emulsion by manually shaking a toluene solution of (S94-*b*-V99)$_4$ in a pH=0.65 aqueous phase. We then directly placed

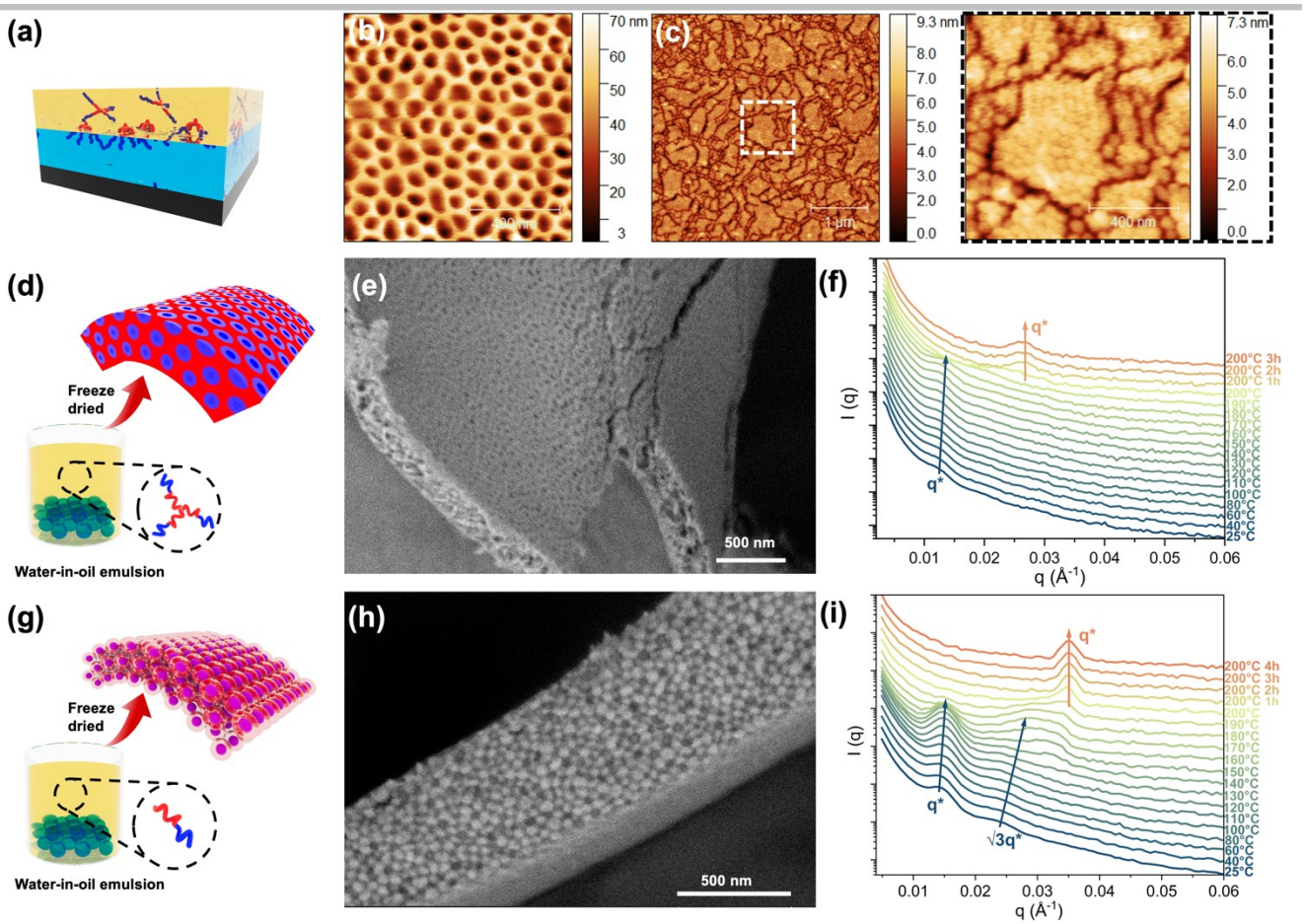

Figure 5. Large-scale nanoporous films are derived from distinct interfacial assembly pathways. a) Schematic depiction of direct preparation of interfacial assemblies on a silicon substrate. b) Nanoporous film and c) large domains from assemblies of hard spherical micelles of 4-arm s-BCPs. For b), the aqueous phase was first applied to the wafer, followed by the addition of the toluene phase. The process for c) was carried out in reverse order. Freeze-dried emulsion derived from 3-arm s-BCPs is shown in d) schematic illustration, e) scanning electron microscopy (SEM) image (backscattering detector), and f) temperature-dependent small-angle X-ray scattering (SAXS) of the resultant emulsion assemblies. Freeze-dried emulsion derived from linear diblock BCPs is represented in g) schematic illustration, h) SEM image (backscattering detector), and i) temperature-dependent SAXS of the resultant emulsion assemblies. Linear diblock BCPs (S125-*b*-V124)$_1$, 3-arm BCPs (S98-*b*-V103)$_3$, and 4-arm BCPs (S94-*b*-V99)$_4$ were used in this study. For a)-c), a solution of 0.1 mg/ml s-BCPs in toluene was used, and for d)-i), a solution of 10 mg/ml s-BCPs or linear BCP was used. Both were combined with an aqueous solution of pH 0.65 (adjusted using HCl). After 1 h of s-BCP or linear BCP assembly at the fluid interface, the interfacial assemblies were either air-dried (for a-c) or freeze-dried (for d-i). The SAXS intensity profiles are vertically shifted for clarity.

emulsion droplets onto a silica wafer and air-dried the droplet. As shown in Figure S17, after drying, s-BCPs assemblies maintain an integrity of the emulsion film and form wrinkles, demonstrating the strong binding energy of s-BCPs to fluid interfaces that withstand the air-drying process. Subsequently, we directly imaged the surface of the emulsion droplet by AFM, where the nanoporous structure on the emulsion film was observed. However, this structure was less ordered than that obtained by the interfacial transfer process, due to the collapse of the emulsion droplets during drying.

In addition to air-drying, we freeze-dried emulsion solutions using 10 mg/ml (S150-*b*-V162)$_3$. Surprisingly, the interfacial assemblies were resilient and withstood the freeze-drying process, preserving the continuous emulsion film and yielding a well-defined layer thickness. The MWs of the PS and P2VP are below the entanglement MW (Figure 5e), resulting in cracks in the film.[28] Such brittleness is routinely seen for low molecular weight PS films, due to the absence of entanglements.[29] From the SEM image using a backscattering electron detector (Figure 5e), the pores are seen to be hexagonally packed throughout the film in three dimensions and are identical on both sides of the emulsion film (Figure S18). SAXS absolute intensity measurements confirmed that the hexagonal packing originates from the s-BCPs matrix and air pores, rather than from PS and P2VP, since the absolute scattering intensity of the dried emulsion film was at least one order higher than the bulk (Figure S19). After thermal compression, as shown in Figure S6, SAXS of the emulsion film had interferences at $1:\sqrt{3}$ at room temperature, confirming hexagonal packing. This was

not as evident in Figure 5f due to heating. The d-spacing was calculated to be 50 nm. With heating the emulsion assemblies, the q* gradually shifted from 0.0126 $Å^{-1}$ (50 nm) to 0.0137 $Å^{-1}$ (46 nm) as the temperature increased from 25 °C to 200°C. After holding the temperature at 200°C, another interference emerged at q*=0.0267 $Å^{-1}$ (24 nm), corresponding to the period of the PS-*b*-P2VP microphase separation in the bulk while the interference arising from the porous structure vanished (Figure S20). We note that the films from freeze-dried emulsions can be easily scaled-up to the gram scale, which is only limited by the amount of star BCP available (Figure S21). For linear PS-*b*-P2VP subjected to the same protocol (Figure 5g), the emulsion film is inverted. As seen in the cross-section of the emulsion film in the SEM image with a backscattered electron detector (Figure 5h), linear diblock BCPs form spherical micelles that pack into multilayers at the interface. These spherical micelles are rigid. Thus, they can hexagonally order in 3 dimensions, forming a quasi-crystalline morphology commonly seen with hard nanoparticles (like Silica) system.[30] Temperature-dependent SAXS (Figure 5i) shows that linear diblock BCPs interfacial assemblies had interferences of $1:\sqrt{3}$ at room temperature, with contrast from s-BCPs and air (Figure S19). By heating up from 25 °C to 200 °C, q* shifted from 0.0143 $Å^{-1}$ to 0.0151 $Å^{-1}$, corresponding to a d-spacing change from 44 nm to 42 nm. As the temperature was maintained at 200 °C, the air was removed from the emulsion film, causing a transition in SLD contrast from the s-BCPs and air to PS and P2VP (Figure S20).

Conclusion

We studied the phase behavior of star block copolymer (s-BCPs), having PS as the core block and P2VP as corona block, that were assembled at fluid interfaces by transferring the equilibrated interfacial to a silicon wafer. The interaction between P2VP and the aqueous phase ($\chi_{P2VP\text{-}solvent}$) and P2VP between PS ($\chi_{P2VP\text{-}PS}$) was varied by adjusting the pH of the aqueous phase. At neutral and 3.10 pH, s-BCPs form bicontinuous films but with swapped phases. At pH=0.65, thicker films (~hundreds nm) of interfacial assemblies produced a nanoporous film with hexagonal order, while thinner s-BCPs films (~10 nm) yielded nanotubular structures (both linear and rings) with Q-P2VP as corona and PS as cores. The mechanisms of the formation of these different morphologies were investigated by SAXS, TEM, and cross-section SEM. Variation of the mass concentrations, volume fractions, MWs, and architectures of s-BCPs allowed detailed control over pore size, d-spacing, and tubule diameter. With linear diblock copolymer, the morphologies were inverted, resulting in rigid spherical micelles that order into large grains, where Q-P2VP comprises the core and PS consists of the corona. Large-scale nanoporous films were also produced by freeze drying emulsions, generating films with hexagonally packed pores in the s-BCPs matrix. Temperature-dependence SAXS showed that these structures are kinetically trapped. The emulsion assemblies are inverted using linear diblock copolymer, where hard spherical micelles crystalize in three-dimensions with hexagonal order. This study provides valuable insights into the phase behavior of charged s-BCPs at the fluid interface under the influence of block-block/solvent interactions and BCP architecture. It also offers a facile method for preparing highly ordered nanoporous films with two types of pore structure and finely controlled pores characters, which showed promising applications in nanotemplating, catalysis, membranes, and energy storage and conversion.

Supporting Information

The authors have cited additional references within the Supporting Information.[16a]

Acknowledgements

This work is supported by the Army Research Office under Contract No. W911NF-17-1-0003.

Keywords: Block Copolymer • Interfaces • Morphology • Architecture • Phase Behavior

[1] R. A. Segalman, *Materials Science and Engineering: R: Reports* **2005**, *48*, 191-226.

[2] J. Bang, U. Jeong, Y. Ryu du, T. P. Russell, C. J. Hawker, *Adv Mater* **2009**, *21*, 4769-4792.

[3] W. A. Phillip, B. O'Neill, M. Rodwogin, M. A. Hillmyer, E. L. Cussler, *ACS Appl Mater Interfaces* **2010**, *2*, 847-853.

[4] M. Stefik, S. Guldin, S. Vignolini, U. Wiesner, U. Steiner, *Chem Soc Rev* **2015**, *44*, 5076-5091.

[5] Y. Mai, A. Eisenberg, *Chem Soc Rev* **2012**, *41*, 5969-5985.

[6] P. Mansky, Y. Liu, E. Huang, T. P. Russell, C. Hawker, *Science* **1997**, *275*, 1458-1460.

[7] S. H. Kim, M. J. Misner, T. Xu, M. Kimura, T. P. Russell, *Advanced Materials* **2004**, *16*, 226-231.

[8] a) D. G. Walton, G. J. Kellogg, A. M. Mayes, P. Lambooy, T. P. Russell, *Macromolecules* **2002**, *27*, 6225-6228; b) M. Q. Hu, X. D. Li, W. T. Heller, W. Bras, J. Rzayev, T. P. Russell, *Macromolecules* **2023**, *56*, 2418-2428.

[9] S. H. Anastasiadis, T. P. Russell, S. K. Satija, C. F. Majkrzak, *Phys Rev Lett* **1989**, *62*, 1852-1855.

[10] T. P. Russell, *Current Opinion in Colloid & Interface Science* **1996**, *1*, 107-115.

[11] a) C. Creton, E. J. Kramer, C. Y. Hui, H. R. Brown, *Macromolecules* **2002**, *25*, 3075-3088; b) T. P. Russell, A. Menelle, W. A. Hamilton, G. S. Smith, S. K. Satija, C. F. Majkrzak, *Macromolecules* **2002**, *24*, 5721-5726; c) B. Bernard, H. R. Brown, C. J. Hawker, A. J. Kellock, T. P. Russell, *Macromolecules* **1999**, *32*, 6254-6260.

[12] a) T. P. Russell, S. H. Anastasiadis, A. Menelle, G. P. Felcher, S. K. Satija, *Macromolecules* **2002**, *24*, 1575-1582; b) T. P. Russell, *Materials Science Reports* **1990**, *5*, 171-271.

[13] T. P. Russell, A. M. Mayes, V. R. Deline, T. C. Chung, *Macromolecules* **2002**, *25*, 5783-5789.

[14] a) K. H. Dai, J. Washiyama, E. J. Kramer, *Macromolecules* **2002**, *27*, 4544-4553; b) P. F. Green, T. P. Russell, *Macromolecules* **2002**, *24*, 2931-2935.

[15] M. Hu, T. P. Russell, *Materials Chemistry Frontiers* **2021**, *5*, 1205-1220.

[16] a) J. Y. Carrillo, Z. Chen, U. I. Premadasa, C. Steinmetz, E. B. Coughlin, B. Doughty, T. P. Russell, B. G. Sumpter, *Nanoscale* **2023**, *15*, 1042-1052; b) F. Jimenez-Angeles, H. K. Kwon, K. Sadman, T. Wu, K. R. Shull, M. Olvera de la Cruz, *ACS Cent Sci* **2019**, *5*, 688-699.

[17] Z. Chen, M. Hu, X. Li, D. M. Smith, H. G. Seong, T. Emrick, J. Rzayev, T. P. Russell, *Angew Chem Int Ed Engl* **2022**, *61*, e202201392.

[18] Y. Chai, A. Lukito, Y. Jiang, P. D. Ashby, T. P. Russell, *Nano Lett* **2017**, *17*, 6453-6457.

[19] M. Reifarth, M. Bekir, A. M. Bapolisi, E. Titov, F. Nusshardt, J. Nowaczyk, D. Grigoriev, A. Sharma, P. Saalfrank, S. Santer, M. Hartlieb, A. Boker, *Angew Chem Int Ed Engl* **2022**, *61*, e202114687.

[20] A. Salonen, D. Langevin, P. Perrin, *Soft Matter* **2010**, *6*. 5308-5311.

[21] A. Alkan, S. Wald, B. Louage, B. G. De Geest, K. Landfester, F. R. Wurm, *Langmuir* **2017**, *33*, 272-279.

[22] a) H. G. Seong, Z. Chen, T. Emrick, T. P. Russell, *Angew Chem Int Ed Engl* **2022**, *61*, e202200530; b) H. G. Seong, Z. Fink, Z. Chen, T. Emrick, T. P. Russell, *ACS Nano* **2023**, *17*, 14731-14741.

[23] a) J. M. Ren, T. G. McKenzie, Q. Fu, E. H. Wong, J. Xu, Z. An, S. Shanmugam, T. P. Davis, C. Boyer, G. G. Qiao, *Chem Rev* **2016**, *116*, 6743-6836; b) Z. Li, M. Tang, S. Liang, M. Zhang, G. M. Biesold, Y. He, S.-M. Hao, W. Choi, Y. Liu, J. Peng, Z. Lin, *Progress in Polymer Science* **2021**, *116*, 101387-101444; c) G. Xie, M. R. Martinez, M. Olszewski, S. S. Sheiko, K. Matyjaszewski, *Biomacromolecules* **2019**, *20*, 27-54.

[24] Q. Yuan, T. P. Russell, D. Wang, *Macromolecules* **2020**, *53*, 10981-10987.

[25] J. G. Kennemur, *Macromolecules* **2019**, *52*, 1354-1370.

[26] Z. Sun, W. Zhang, S. Hong, Z. Chen, X. Liu, S. Xiao, E. B. Coughlin, T. P. Russell, *Polymer* **2017**, *121*, 297-303.

[27] X. Liu, S. Shi, Y. Li, J. Forth, D. Wang, T. P. Russell, *Angew Chem Int Ed Engl* **2017**, *56*, 12594-12598.

[28] B. S. Tomar, A. Shahin, M. S. Tirumkudulu, *Soft Matter* **2020**, *16*, 3476-3484.

[29] S. Zhang, M. Koizumi, Z. Cao, K. S. Mao, Z. Qian, L. A. Galuska, L. Jin, X. Gu, *ACS Polym Au* **2021**, *1*, 16-29.

[30] P. Y. Kim, Y. Gao, Z. Fink, A. E. Ribbe, D. A. Hoagland, T. P. Russell, *ACS Nano* **2022**, *16*, 5496-5506.

Entry for the Table of Contents

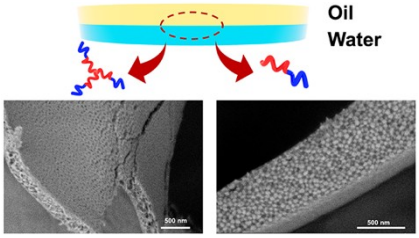

Table of Contents text:

The phase behaviors of block copolymers (BCPs) at fluids interface were studied, where a series of star block copolymers (s-BCPs) with polystyrene (PS) as core and poly(2-vinylpyridine) (P2VP) as corona were synthesized. s-BCPs showed hexagonal-packed nanoporous film with s-BCP comprising matrix. The morphology of linear BCPs were inverted, where hexagonal-packed rigid spherical micelles of BCP form multilayer.